

Chapter 6

Guided wave focusing in viscoelastic multilayered hollow cylinders

The problem of free waves in viscoelastic multilayered hollow cylinders now has been solved. In many practical problems, transducers have to be mounted on the surface in order to send ultrasonic energy into the cylinders. Changing surface conditions affects the ultrasonic energy source and hence mode types; commonly known as “source influence.” Similar to the source influence problem in single-layered elastic hollow cylinders, Normal Mode Expansion (NME) can be used as a potent tool to solve the source influence problem in viscoelastic multilayered hollow cylinders. The process of solving the source influence problem in multilayered hollow cylinders is similar to that in a single layered elastic hollow cylinder. The difference lies in the fact that the whole derivation is based upon the real reciprocity relation and one needs to make use of the interfacial displacement and normal stress continuity conditions for the viscoelastic multilayered case, while the derivation for the single-layered elastic case is based on the complex reciprocity relation but no interfacial conditions are considered. These differences also correspond to the differences in the derivation of the orthogonality relations for viscoelastic multilayered cylinders and single-layered elastic cylinders.

6.1 Source influence

Consider the wave field generated by a finite source to be a superposition of all the normal modes in a viscoelastic coated hollow cylinder. This generated wave field is chosen to be solution “1” in the reciprocity relation (Eq. 5.17). The displacement vector and stress tensor of the generated wave field can be expanded as follows

$$\mathbf{v}_1 = \mathbf{v} = \sum_{N=0}^{\infty} \sum_{\mu} A_{\mu}^N(z) \mathbf{v}_{\mu}^N(r, \theta), \quad 6.1$$

and

$$\mathbf{T}_1 = \mathbf{T} = \sum_{N=0}^{\infty} \sum_{\mu} A_{\mu}^N(z) \mathbf{T}_{\mu}^N(r, \theta), \quad 6.2$$

where N is the circumferential order, μ is the group index, and $A_{\mu}^N(z)$ is the amplitude of the normal mode (N, μ) obtained from NME method. The normal mode n of circumferential order M is chosen to be solution “2” in the reciprocity relation. The expressions are given in Eq. 6.3 and Eq. 6.4.

$$\mathbf{v}_2 = \mathbf{v}_n^M(r, \theta) e^{-i\beta_n^M z} \quad 6.3$$

$$\mathbf{T}_2 = \mathbf{T}_n^M(r, \theta) e^{-i\beta_n^M z} \quad 6.4$$

Then we have

$$\mathbf{v}_1 \cdot \mathbf{T}_2 = \sum_{N=0}^{\infty} \sum_{\mu} A_{\mu}^N(z) \mathbf{v}_{\mu}^N(r, \theta) \cdot \mathbf{T}_n^M(r, \theta) e^{-i\beta_n^M z}, \quad 6.5$$

$$\mathbf{v}_2 \cdot \mathbf{T}_1 = \sum_{N=0}^{\infty} \sum_{\mu} A_{\mu}^N(z) \mathbf{v}_n^M(r, \theta) \cdot \mathbf{T}_{\mu}^N(r, \theta) e^{-i\beta_n^M z}. \quad 6.6$$

Subtracting Eq. 6.6 from Eq. 6.5 gives

$$\begin{aligned}
& \mathbf{v}_1 \cdot \mathbf{T}_2 - \mathbf{v}_2 \cdot \mathbf{T}_1 \\
&= \sum_{N=0}^{\infty} \sum_{\mu} A_{\mu}^N(z) [\mathbf{v}_{\mu}^N(r, \theta) \cdot \mathbf{T}_n^M(r, \theta) - \mathbf{v}_n^M(r, \theta) \cdot \mathbf{T}_{\mu}^N(r, \theta)] e^{-i\beta_n^M z} .
\end{aligned} \tag{6.7}$$

Substituting Eq. 6.7 into the reciprocity relation Eq. 5.17, we obtain

$$\begin{aligned}
& \nabla_{r\theta} \cdot [\mathbf{v}_1 \cdot \mathbf{T}_n^M(r, \theta) - \mathbf{v}_n^M(r, \theta) \cdot \mathbf{T}_1] e^{-i\beta_n^M z} \\
&+ \frac{\partial}{\partial z} \left\{ \sum_{N=0}^{\infty} \sum_{\mu} A_{\mu}^N(z) [\mathbf{v}_{\mu}^N(r, \theta) \cdot \mathbf{T}_n^M(r, \theta) - \mathbf{v}_n^M(r, \theta) \cdot \mathbf{T}_{\mu}^N(r, \theta)] \cdot \hat{\mathbf{e}}_z e^{-i\beta_n^M z} \right\} = 0 .
\end{aligned} \tag{6.8}$$

Integrating the preceding equation over the cross section of the cylinder D and making use of the definition of $P_{\mu m}^{NM}$, Eq. 6.8 becomes

$$\begin{aligned}
& e^{-i\beta_n^M z} \iint_D \nabla_{r\theta} \cdot [\mathbf{v}_1 \cdot \mathbf{T}_n^M(r, \theta) - \mathbf{v}_n^M(r, \theta) \cdot \mathbf{T}_1] d\sigma \\
&= 4 \frac{\partial}{\partial z} \left\{ \sum_{N=0}^{\infty} \sum_{\mu} A_{\mu}^N(z) P_{\mu m}^{NM} e^{-i\beta_n^M z} \right\} .
\end{aligned} \tag{6.9}$$

Eq. 6.9 can be convert to

$$\begin{aligned}
& \iint_D \nabla_{r\theta} \cdot [\mathbf{v}_1 \cdot \mathbf{T}_n^M(r, \theta) - \mathbf{v}_n^M(r, \theta) \cdot \mathbf{T}_1] d\sigma \\
&= 4 e^{i\beta_n^M z} \frac{\partial}{\partial z} \left\{ \sum_{N=0}^{\infty} \sum_{\mu} A_{\mu}^N(z) P_{\mu m}^{NM} e^{-i\beta_n^M z} \right\} .
\end{aligned} \tag{6.10}$$

Letting

$$\{\} = \mathbf{v}_1 \cdot \mathbf{T}_n^M(r, \theta) - \mathbf{v}_n^M(r, \theta) \cdot \mathbf{T}_1, \tag{6.11}$$

the left hand side of Eq. 6.10 becomes Eq. 6.12 and after some mathematical manipulation as done in the previous chapter for the derivation of orthogonality,

$$\iint_D \nabla_{r\theta} \cdot \{\} d\sigma = \oint_{\partial_1 D} \hat{\mathbf{n}}_1 \cdot \{\} ds + \oint_{\partial_2 D} \hat{\mathbf{n}}_2 \cdot \{\} ds + \oint_{\partial_2 D} \hat{\mathbf{n}}_1 \cdot \{\} ds + \oint_{\partial_3 D} \hat{\mathbf{n}}_2 \cdot \{\} ds . \tag{6.12}$$

In Eq. 6.12, D_1 and D_2 denote the cross sections of the elastic hollow cylinder and the viscoelastic coating respectively. $\partial_1 D$ represents the inner boundary of D_1 , $\partial_2 D$

represents the interface between D_1 and D_2 , and $\partial_3 D$ represents the outer boundary of D_2 . The direction vectors $\hat{\mathbf{n}}_1$ and $\hat{\mathbf{n}}_2$ are defined in Eq. 5.25.

Making use of the identities

$$\hat{\mathbf{n}}_1 \cdot [\mathbf{v}_1 \cdot \mathbf{T}_n^M(r, \theta) - \mathbf{v}_n^M(r, \theta) \cdot \mathbf{T}_1] = \mathbf{v}_1 \cdot (\hat{\mathbf{n}}_1 \cdot \mathbf{T}_n^M(r, \theta)) - \mathbf{v}_n^M(r, \theta) \cdot (\hat{\mathbf{n}}_1 \cdot \mathbf{T}_1), \quad 6.13$$

$$\hat{\mathbf{n}}_2 \cdot [\mathbf{v}_1 \cdot \mathbf{T}_n^M(r, \theta) - \mathbf{v}_n^M(r, \theta) \cdot \mathbf{T}_1] = \mathbf{v}_1 \cdot (\hat{\mathbf{n}}_2 \cdot \mathbf{T}_n^M(r, \theta)) - \mathbf{v}_n^M(r, \theta) \cdot (\hat{\mathbf{n}}_2 \cdot \mathbf{T}_1), \quad 6.14$$

and noticing that the displacements and normal stresses are continuous at the interface $\partial_2 D$, Eq. 6.12 is simplified to

$$\begin{aligned} \iint_D \nabla_{r\theta} \cdot \{\} d\sigma &= \oint_{\partial_1 D} \{\mathbf{v}_1 \cdot (\hat{\mathbf{n}}_1 \cdot \mathbf{T}_n^M(r, \theta)) - \mathbf{v}_n^M(r, \theta) \cdot (\hat{\mathbf{n}}_1 \cdot \mathbf{T}_1)\} ds \\ &+ \oint_{\partial_3 D} \{\mathbf{v}_1 \cdot (\hat{\mathbf{n}}_2 \cdot \mathbf{T}_n^M(r, \theta)) - \mathbf{v}_n^M(r, \theta) \cdot (\hat{\mathbf{n}}_2 \cdot \mathbf{T}_1)\} ds \end{aligned} \quad 6.15$$

Also notice that the tractions produced by the normal modes vanish at the inner and outer boundaries, Eq. 6.15 can be further reduced to

$$\iint_D \nabla_{r\theta} \cdot \{\} d\sigma = -\oint_{\partial_1 D} \mathbf{v}_n^M(r, \theta) \cdot (\hat{\mathbf{n}}_1 \cdot \mathbf{T}_1) ds - \oint_{\partial_3 D} \mathbf{v}_n^M(r, \theta) \cdot (\hat{\mathbf{n}}_2 \cdot \mathbf{T}_1) ds. \quad 6.16$$

From Eq. 6.10 and Eq. 6.16, we obtain

$$\begin{aligned} &4e^{i\beta_n^M z} \frac{\partial}{\partial z} \left\{ \sum_{N=0}^{\infty} \sum_{\mu} A_{\mu}^N(z) P_{\mu m}^{NM} e^{-i\beta_n^M z} \right\} \\ &= -\oint_{\partial_1 D} \mathbf{v}_n^M(r, \theta) \cdot (\hat{\mathbf{n}}_1 \cdot \mathbf{T}_1) ds - \oint_{\partial_3 D} \mathbf{v}_n^M(r, \theta) \cdot (\hat{\mathbf{n}}_2 \cdot \mathbf{T}_1) ds \end{aligned} \quad 6.17$$

From the orthogonality relation Eq. 5.32, the only non-zero term on the left hand side of Eq. 6.17 is

$$\begin{aligned} &4e^{i\beta_n^M z} \frac{\partial}{\partial z} \left\{ A_{-n}^M(z) P_{-nm}^{MM} e^{-i\beta_n^M z} \right\} \\ &= -\oint_{\partial_1 D} \mathbf{v}_n^M(r, \theta) \cdot (\hat{\mathbf{n}}_1 \cdot \mathbf{T}_1) ds - \oint_{\partial_3 D} \mathbf{v}_n^M(r, \theta) \cdot (\hat{\mathbf{n}}_2 \cdot \mathbf{T}_1) ds \end{aligned} \quad 6.18$$

where P_{-nm}^{MM} is from the two modes with wave numbers β_n^M and $-\beta_n^M$. For traction loading on the inner boundary, we obtain

$$4P_{-nm}^{MM} \left(\frac{\partial}{\partial z} - i\beta_n^M \right) A_{-n}^M(z) = -\oint_{\partial_1 D} \mathbf{v}_n^M(r, \theta) \cdot (\hat{\mathbf{n}}_1 \cdot \mathbf{T}_1) ds. \quad 6.19$$

For convenience, interchange n and $-n$, β_n^M and $-\beta_n^M$, we get

$$4P_{n(-n)}^{MM} \left(\frac{\partial}{\partial z} + i\beta_n^M \right) A_n^M(z) = -\oint_{\partial_1 D} \mathbf{v}_{-n}^M(r, \theta) \cdot (\hat{\mathbf{n}}_1 \cdot \mathbf{T}_1) ds. \quad 6.20$$

Solving the above equation yields the amplitude factors of the generated normal modes

$$A_n^M = -\frac{e^{-i\beta_n^M z}}{4P_{n(-n)}^{MM}} \int_{-\infty}^z e^{i\beta_n^M \eta} \left\{ \oint_{\partial_1 D} \mathbf{v}_{-n}^M(r, \theta) \cdot (\hat{\mathbf{n}}_1 \cdot \mathbf{T}_1) ds \right\} d\eta \quad 6.21$$

6.2 Focusing in multilayered viscoelastic hollow cylinders

After the source influence problem is solved, the computation of focusing parameters in multilayered viscoelastic hollow cylinders follows closely to that in single layered hollow cylinders as described in Chapter 3. The transducer location for the source influence in the previous section was assumed to be the inner surface of the pipe. In applications, guided wave focusing in pipes is usually conducted at relatively low frequencies. It is found that, at low frequencies, the dominant displacement and stress distribution are mostly uniform across the thickness. Applying the traction on either the inner surface, outer surface or the interface of the coated pipe does not make a significant

influence in resulting angular profiles and focusing parameters. What is needed to be pointed out here is that the outer surface of the pipe section corresponds to the interface between the pipe and the coating. Sometimes if the coating is very viscous, a small area of the coating can be removed from the pipe to get better coupling between the transducer arrays and the pipe. In this case, part of the energy excited in the bare pipe will be reflected when impinged onto the coated pipe. However, the angular profiles in this work are assumed not to be affected by the reflection between the bare pipe and the coated pipe. The displacement and stress field distribution in bare pipes are almost the same as the displacement and stress field distribution in the pipe section in a coated pipe over low frequency range. This can be observed from the previous calculation on wave structures of the same mode (for example, $L(0,2)$) in bare pipes (Figure 2-8 in Chapter 2) and in coated pipes (Figure 5-8 Chapter 5). Because of the match in the field distributions between bare pipes and the coated pipes, the influence of reflection on the wave incident from a bare pipe into a coated pipe can be neglected.

6.2.1 Focusing in a single layered elastic hollow cylinder: SAFE vs. analytical GMM

Due to the fact that finite element approximation is used in at least one dimension or two over the cross section of the wave guide in the SAFE method, there have existed some doubts on how accurate the SAFE calculation can be in such a problem of guided wave propagation and focusing in hollow cylinders. Although we have showed by the dispersion curve figures in the previous chapter that the SAFE calculation of coated pipe dispersion curves match those calculated from the analytical global matrix method

(GMM) very well at low frequency. Quantitative comparison was not provided in the previous chapter. In this chapter, we will compare quantitatively the phase velocities, angular profiles, and focusing parameters calculated from both methods for a single layered elastic hollow cylinder to show that the SAFE method can provide enough accuracy in computing the wave propagation and focusing parameters in hollow cylindrical structures.

The phase velocities of modes $T(n,1)$ for $n=0$ to 10 in an 8 in. schedule 40 steel pipe at a frequency of 60 kHz calculated using the analytical GMM and the SAFE method are listed and compared in Table 6-1. 26 nodes are used in the radial direction across the pipe thickness in the SAFE calculation. Both methods are programmed in MATLAB[®] using double precision. It can be seen from Table 6-1 that the phase velocities calculated from both methods match each other up to 15 digits.

Table 6-1: Phase velocity comparison using the Analytical GMM and the SAFE for modes $T(n,1)$ in an 8 in. schedule 40 steel pipe at a frequency of 60 kHz. The unit of phase velocity is mm/ μ s.

Circumferential order n	Analytical GMM	SAFE
0	3.229999999999498	3.229999999999498
1	3.241024295421381	3.241024295421381
2	3.274761185134115	3.274761185134115
3	3.333318152134975	3.333318152134975
4	3.420633969562764	3.420633969562764
5	3.543289222538042	3.543289222538042
6	3.712104504906446	3.712104504906446
7	3.945415614923628	3.945415614923628
8	4.276416296128982	4.276416296128982
9	4.772104034238862	4.772104034238862
10	5.594113921161920	5.594113921161920

The wave structures of the above torsional flexural modes $T(n,1)$ with $n=1$ to 6 calculated from analytical GMM and SAFE method are plotted and compared in Figure 6-1. The displacement amplitudes in the r , θ , and z directions are plotted in blue, red, and green respectively. Also, different markers and line styles are used to represent the displacement components calculated by the two different methods as shown in the legend in each plot. It can be seen from Figure 6-1 that the wave structures calculated from the analytical GMM and the SAFE method agree with each other very well.

The amplitude factors of the torsional modes group $T(n,1)$ generated by a 45° shear source loading on the 8 in. schedule 40 steel pipe based on the phase velocities and wave structures calculated for the analytical GMM and the SAFE method are plotted in Figure 6-2. As can be seen from Figure 6-2, the amplitude factors calculated from both methods match very well. Only very slight difference can be observed for the amplitude factors of mode $T(1,1)$ and $T(2,1)$.

Some sample angular profiles for the 45° shear source loading and their corresponding 8 channel focused angular profiles calculated based on analytical and SAFE methods are shown in Figure 6-3. The left column shows the partial loading angular profiles and the right column is the corresponding focused profiles at different axial distances in the 8 in. schedule 40 steel pipe at a frequency of 60 kHz. As can be observed from Figure 6-3, the final focused profiles calculated from both analytical and SAFE methods overlap, indicating they agree with each other quite well. A more quantitative comparison of the focusing parameters calculated from both methods for the focused profile at 0.5 m. in Figure 6-3 is given in Table 6-2. The largest difference

between the focusing parameters calculated from both methods is below 0.3% in this case.

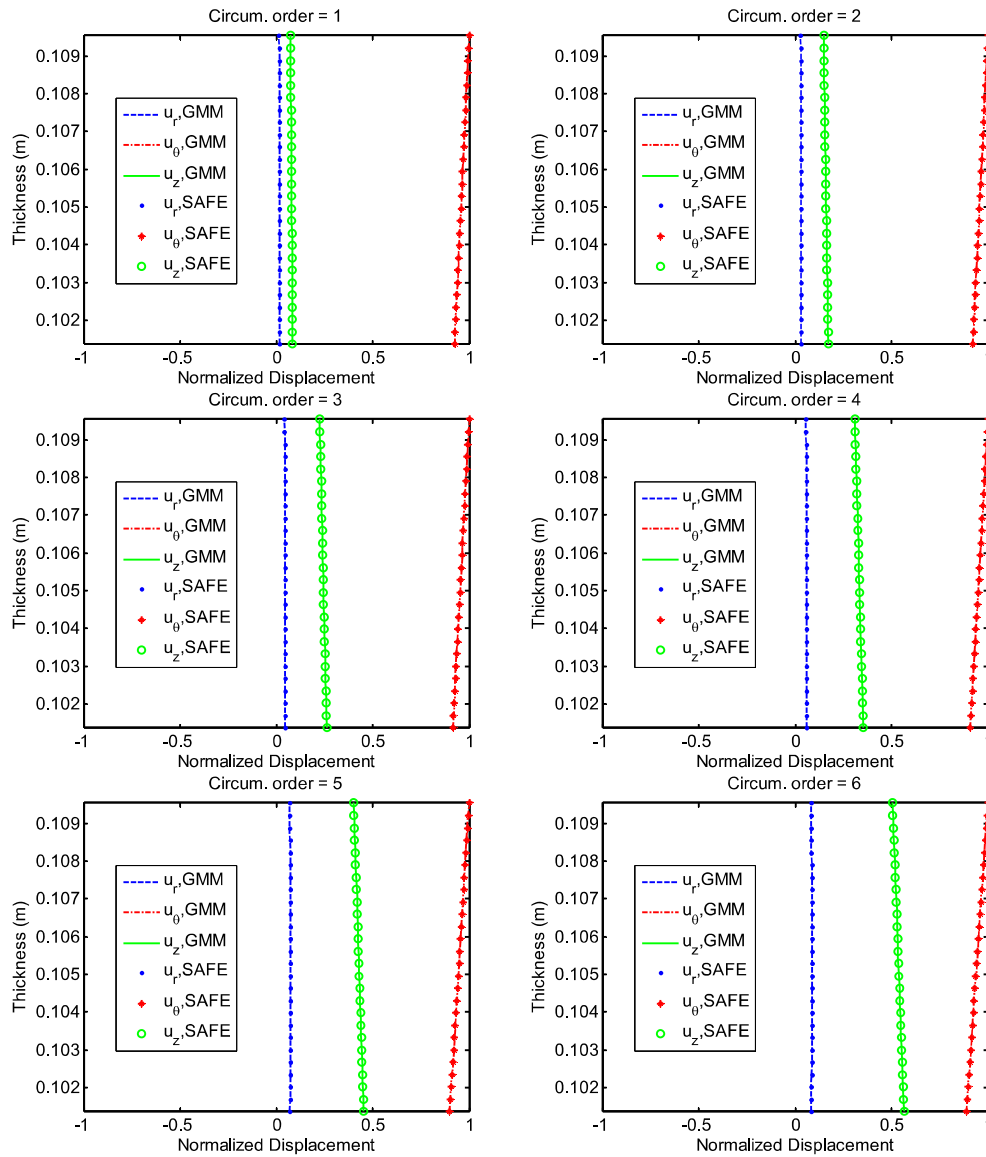


Figure 6-1: Sample wave structure comparison. The wave structures are computed using analytical GMM and the SAFE for modes $T(n,1)$, where circumferential order n equals 1 to 6, in an 8 in. schedule 40 steel pipe at a frequency of 60 kHz.

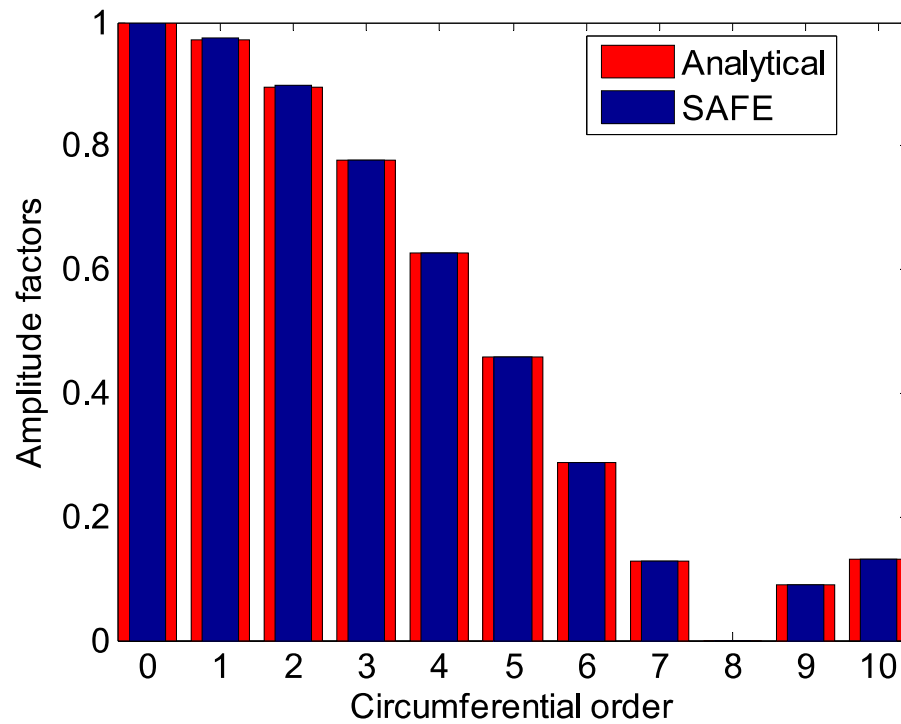


Figure 6-2: Comparison of the amplitude factors computed from the analytical method and SAFE method for a 45° shear partial loading on an 8 in. schedule 40 steel pipe in generating the torsional mode group $T(n,1)$ at 60 kHz. In the figure, the amplitude factors are plotted for circumferential order n from 0 to 10.

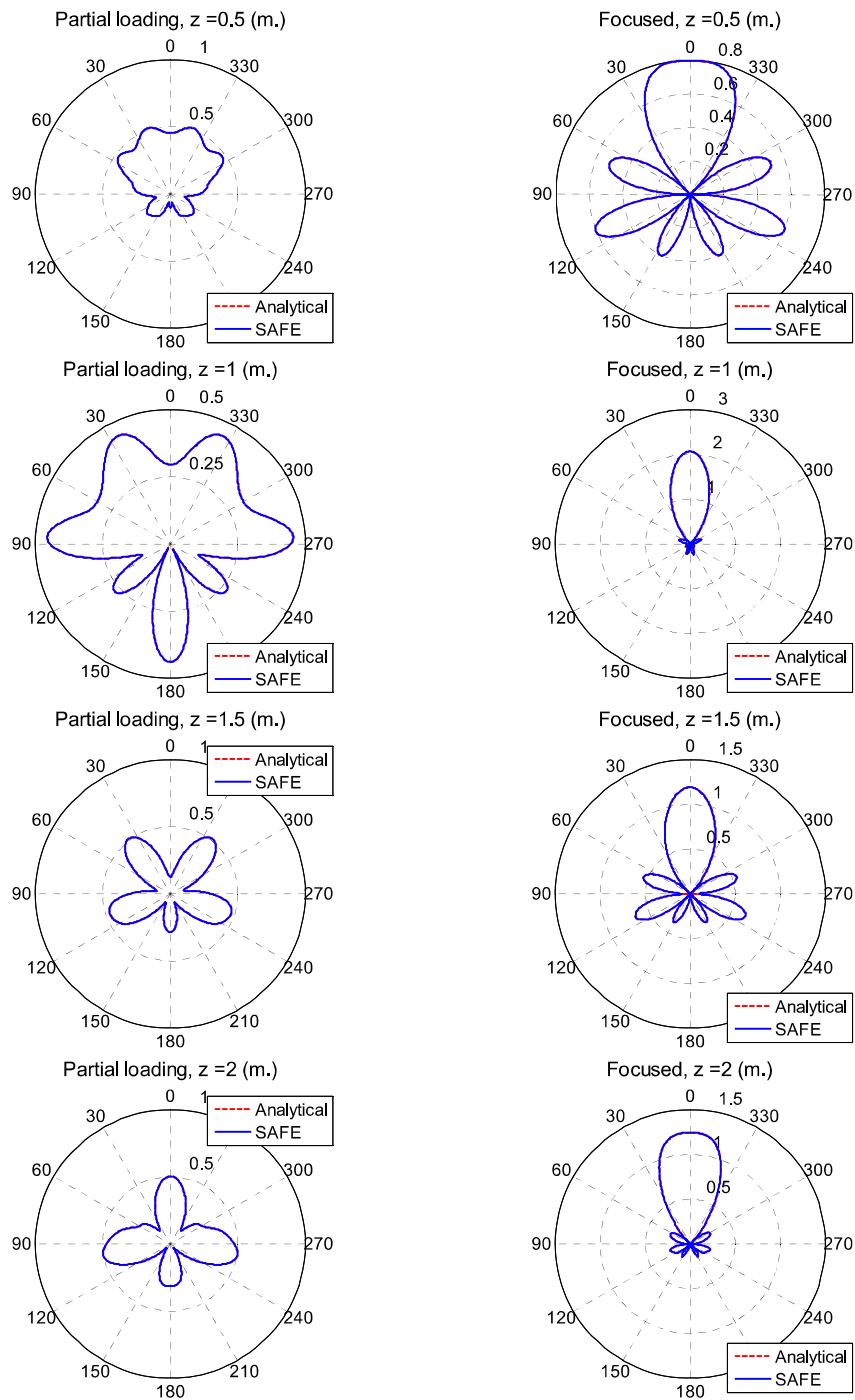


Figure 6-3: Angular profiles of 45° shear partial loading (left column) and their corresponding focused profiles (right column) at different axial distances in an 8 in. schedule 40 steel pipe calculated from analytical and SAFE methods at 60 kHz.

Table 6-2: Comparison of 8 channel focusing parameters in an 8 in. schedule 40 steel pipe at a focal distance of 0.5 m. for torsional modes $T(n,1)$ at 60 kHz. (The focusing parameters correspond to the focused profile on the right hand side in the first row in Figure 6-3.)

Channel #	Analytical		SAFE	
	Amplitude factors	Time delays (μs)	Amplitude factors	Time delays (μs)
1	1.000	14.928	1.000	14.926
2	0.589	9.381	0.589	9.381
3	0.244	5.992	0.244	5.989
4	0.498	16.203	0.497	16.201
5	0.622	6.578	0.621	6.579
6	0.498	16.203	0.497	16.201
7	0.244	5.992	0.244	5.989
8	0.589	9.381	0.589	9.381

The comparison of longitudinal focusing using the analytical method and the SAFE method is also given below. The phase velocities of modes $L(n,2)$ for $n=0$ to 10 in an 8 in. schedule 40 steel pipe at a frequency of 95 kHz calculated using the analytical GMM and the SAFE method are listed in Table 6-3. 26 nodes (the same as the torsional case) are used in the radial direction across pipe thickness in the SAFE calculation. The phase velocities calculated by the two methods are still in very good agreement, although the accuracy is not as good as in the torsional case. The largest difference in the phase velocities calculated by the two methods is less than 0.0013%.

The amplitude factors of the longitudinal modes group $L(n,2)$ generated by a 45° source loading on the 8 in. schedule 40 steel pipe calculated for the analytical GMM and SAFE methods are plotted in Figure 6-4. As can be seen from Figure 6-4, the amplitude factors calculated from both methods match very well.

A sample angular profile for the 45° longitudinal source loading and its corresponding 8 channel focused angular profiles calculated based on analytical and SAFE methods are shown in Figure 6-5. The left plot in Figure 6-5 is the partial loading angular profile and the right one is the corresponding focused profile at an axial distance of 4.6 m. in an 8 in. schedule 40 steel pipe at a 95 kHz. As can be observed from Figure 6-5, the final focused profiles for the longitudinal case calculated from both analytical and SAFE methods agree quite well with each other. A comparison of the focusing parameters calculated from both methods for the focused profile in Figure 6-4 is given in Table 6-4. The largest difference between the focusing parameters calculated from both methods is less than 6%.

Table 6-3: Phase velocity comparison using the Analytical GMM and the SAFE for modes L(n,2) in an 8 in. schedule 40 steel pipe at a frequency of 95 kHz. The unit is mm/μs.

Circumferential order n	Analytical GMM	SAFE
0	5.357340631484985	5.357365912407072
1	5.376876831054688	5.376902395541808
2	5.436795587539673	5.436822058343757
3	5.541280241012573	5.541308335504786
4	5.698246393203736	5.698277055756171
5	5.921181259155273	5.921215842902375
6	6.232908039093018	6.232948667164218
7	6.673722028732300	6.673772352486621
8	7.321066303253174	7.321133528599280
9	8.346378173828125	8.346479261771242
10	10.235868984401089	10.235868984401089

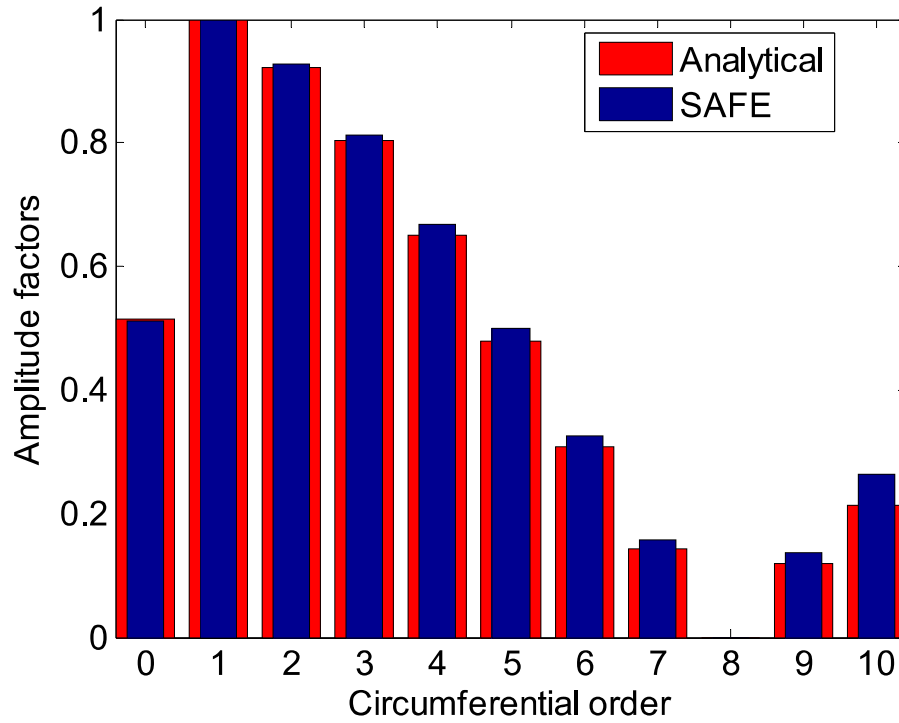


Figure 6-4: Comparison of the amplitude factors computed from the analytical method and SAFE method for a 45° longitudinal partial loading on an 8 in. schedule 40 steel pipe in generating the longitudinal mode group L(n,2) at 95 kHz. In the figure, the amplitude factors are plotted for circumferential order n from 0 to 10.

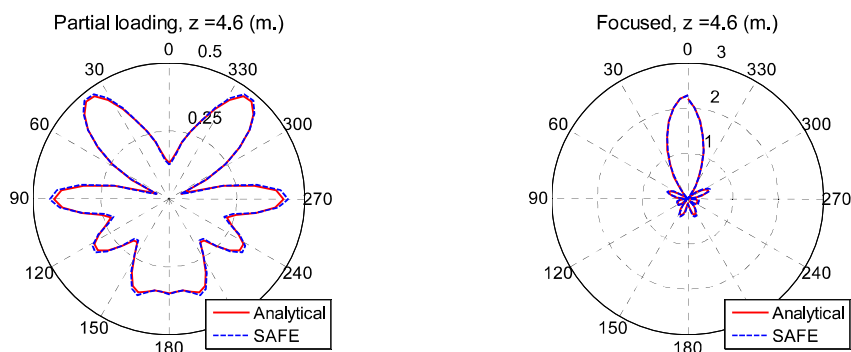


Figure 6-5: Angular profile of 45° longitudinal partial loading (left) and the corresponding focused profile (right) at 4.6 m. in an 8 in. schedule 40 steel pipe calculated from analytical and SAFE methods at 95 kHz.

Table 6-4: Comparison of 8 channel focusing parameters in an 8 in. schedule 40 steel pipe at a focal distance of 4.6 m. for longitudinal modes $L(n,2)$ at 95 kHz. (The focusing parameters correspond to the focused profile on the right hand side in Figure 6-5.)

Channel #	Analytical		SAFE	
	Amplitude factors	Time delays (μs)	Amplitude factors	Time delays (μs)
1	0.617	6.535	0.611	6.589
2	1.000	7.023	1.000	7.019
3	0.933	2.963	0.921	3.025
4	0.686	2.354	0.694	2.370
5	0.678	5.149	0.640	5.065
6	0.686	2.354	0.694	2.370
7	0.933	2.963	0.921	3.025
8	1.000	7.023	1.000	7.019

6.2.2 Focusing in multilayered viscoelastic hollow cylinders using SAFE

The comparison between the focusing in bare pipes using analytical and SAFE methods in the previous chapter shows that the SAFE method is an effective tool in

calculating the focusing amplitude factors and time delays. In this chapter, the SAFE method is used for the calculation of focusing parameters in viscoelastic coated pipes. The method can be generalized in calculating guided wave focusing in other viscoelastic multilayered cylindrical structures also. However, only the numerical calculation of focusing in coated pipes will be given here to demonstrate the technique.

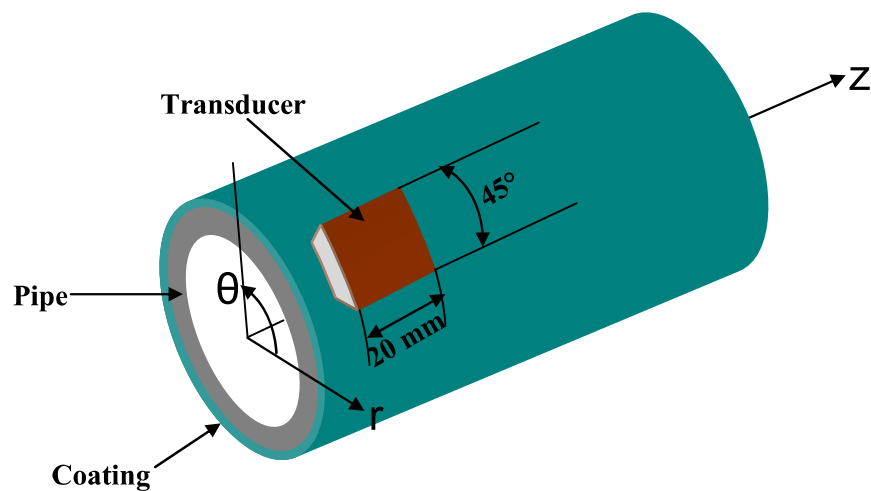


Figure 6-6: Coated pipe with a source loading covering 45° in circumferential direction and 20 mm. in axial direction.

Consider a transducer array covering 45° in the circumferential direction vibrating in the axial direction on the outer surface of an 8 in. schedule 40 steel pipe (Figure 6-6). The pipe is coated with 2 mm thick E&C 2057 / Cat9 epoxy. The material properties can be found in Table 5-1. The total field generated by such a partial source loading can be calculated from the amplitude factors of the generated guided wave modes and their superposition. The generated guided wave modes in this case are mostly the longitudinal modes $L(n,2)$. Theoretically speaking, the other longitudinal mode group $L(n,1)$ ($n > 0$), which has small displacement in the z direction, will be generated as well, but with much

smaller amplitudes compared to the generated $L(n,2)$ modes. In addition, the group velocities of the $L(n,1)$ and the $L(n,2)$ modes are very different from each other. In practice, most likely these two mode groups will not reach the focal position at the same time if the exciting signal is a toneburst. Therefore, the displacement angular profiles are only calculated based on the summation of the $L(n,2)$ modes only. The particle displacement angular profiles of the generated field at the interface between the pipe and the coating are shown in the left column of Figure 6-7. Their corresponding 8 channel focused profiles are given in the right column respectively. As shown in Figure 6-7, the angular profiles are plotted at difference sample distances and at a frequency of 120 kHz.

It can be observed from Figure 6-7 that, similar to bare pipes, the angular profile changes with distance in viscoelastic coated pipes due to the difference in phase velocities of the generated modes. Angular profiles are results of the constructive and destructive interference among the wave modes around the pipe circumference. Because the phase velocities vary with frequency, the angular profiles and focusing parameters change with frequency correspondingly.

The angular profile tuning of the torsional modes $T(n,1)$ can be achieved in the same way as longitudinal modes except that the transducer vibration direction should be in the circumferential direction in order to generate the $T(n,1)$ modes. Using the transducers vibrating in the circumferential direction of the pipe coincides with the dominant displacement direction of the torsional modes $T(n,1)$. Thus, the $T(n,1)$ modes can be largely generated. The displacement angular profiles for the $T(n,1)$ modes generated by 45° normal loading in an 8 in. schedule 40 steel pipe coated with 2-mm E&C 2057 / Cat9 epoxy are illustrated in the left column of Figure 6-8 for different

propagating distances. Their corresponding 8-channel focused profiles are shown in the right column of Figure 6-8. Similar to the longitudinal case, the angular profiles and focusing parameters change with propagating distance and operating frequency.

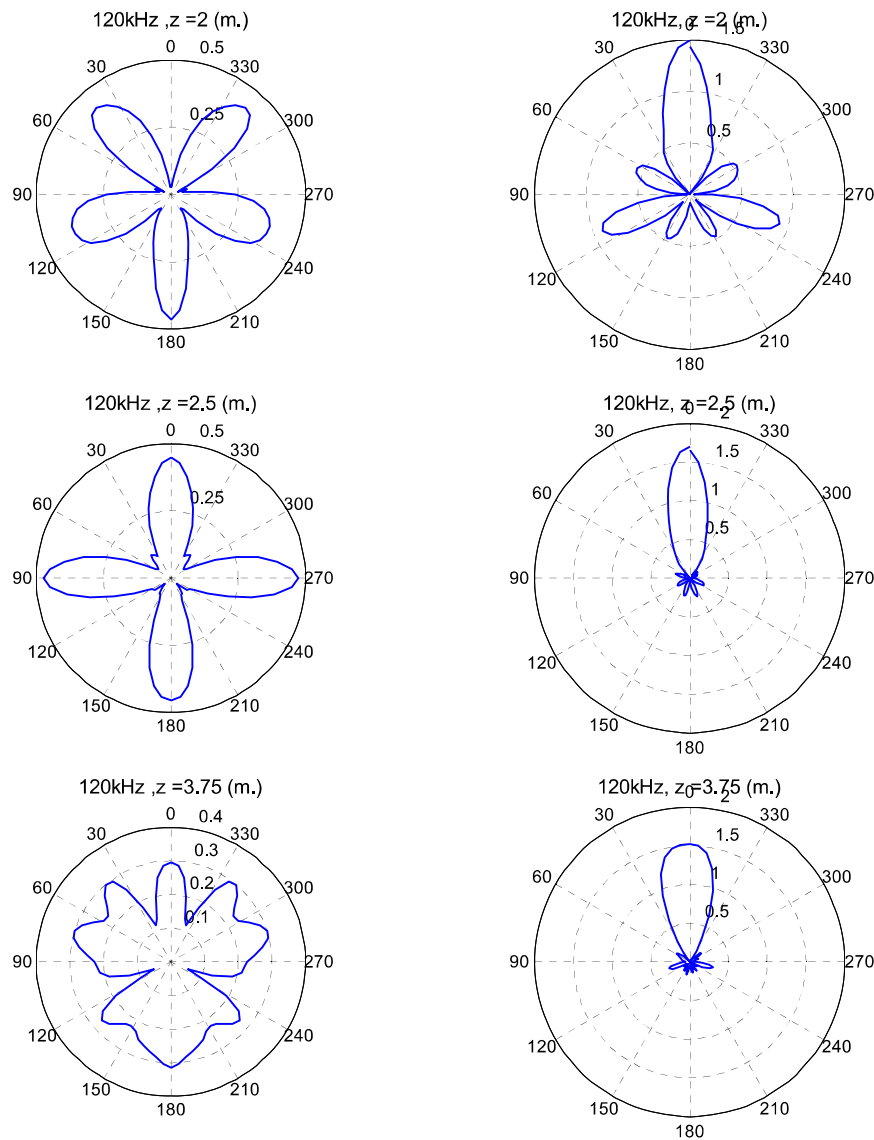


Figure 6-7: The particle displacement angular profiles (left column) and their corresponding focused profiles (right column) at different distances in an 8 in. schedule 40 steel pipe coated with 2-mm E&C 2057 / Cat9 epoxy. L(n,2) modes are generated and 8 channel focusing is used.

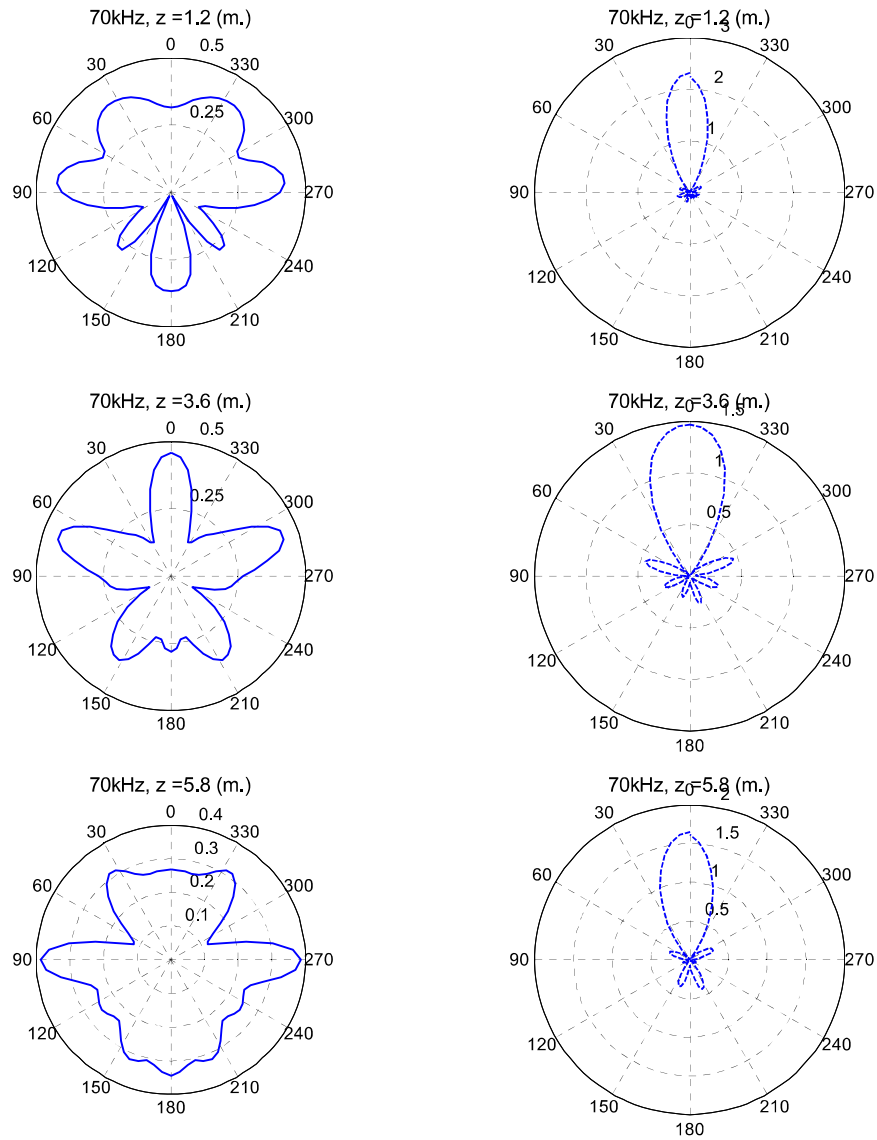


Figure 6-8: The particle displacement angular profiles (left column) and their corresponding focused profiles (right column) at different distances in an 8 in. schedule 40 steel pipe coated with 2-mm E&C 2057 / Cat9 epoxy. T(n,1) modes are generated and 8 channel focusing is used.